

## Triclinic BiFeO<sub>3</sub>: A room-temperature multiferroic phase with enhanced magnetism and resistivity

Md. Sariful Sheikh <sup>1,\*</sup>,<sup>†,‡</sup> Tushar Kanti Bhowmik <sup>1,2,†,§</sup>, Alo Dutta,<sup>2</sup> Sujoy Saha <sup>3</sup>, Chhatra R. Joshi,<sup>4</sup> and T. P. Sinha<sup>1</sup>

<sup>1</sup>Department of Physics, Bose Institute, 93/1 A.P.C. Road, Kolkata 700009, India

<sup>2</sup>Department of Condensed Matter Physics and Material Sciences, S. N. Bose National Centre for Basic Sciences, Block-JD, Sector-III, Salt Lake, Kolkata 700106, India

<sup>3</sup>Department of Physics, Oakland University, Rochester, Michigan 48309, USA

<sup>4</sup>Department of Physics and Astronomy, The University of Alabama, Tuscaloosa, Alabama 35487, USA



(Received 19 November 2022; revised 28 August 2023; accepted 11 September 2023; published 29 September 2023)

The magnetic and transport properties of BiFeO<sub>3</sub>/La<sub>2</sub>NiMnO<sub>6</sub> (BFO/LNMO) composite were investigated both experimentally and theoretically. Unlike the normal rhombohedral (*R3c*) phase, BFO in composites is crystallized in the triclinic phase (*P1*). Interestingly, the composites demonstrate a significant enhancement in magnetization and magnetoelectric coupling and show higher resistivity than regular BFO (*R3c*). As LNMO has its Curie temperature at 280 K, the room temperature and above room temperature magnetic contribution in the composites is expected to be from the triclinic BFO phase. Experimentally observed enhancement in magnetization is validated using classical Monte Carlo simulation and density functional theory (DFT) calculations. The calculations reveal higher magnetic moments in triclinic BFO as compared to the rhombohedral BFO. Overall, this study reveals triclinic BFO as a promising room temperature multiferroic phase which is helpful to optimize the multiferroicity of BFO and achieve wider applications in future.

DOI: [10.1103/PhysRevB.108.104427](https://doi.org/10.1103/PhysRevB.108.104427)

### I. INTRODUCTION

*ABO*<sub>3</sub> type multiferroic perovskite oxide BiFeO<sub>3</sub> has attracted much research attention owing to the rare coexistence of ferroelectric and antiferromagnetic ordering with high transition temperatures (ferroelectric Curie temperature  $T_C \sim 1100$  K and Néel temperature  $T_N \sim 640$  K) [1–3]. Since the initial demonstration of robust coupling between these two order parameters, the promising possibility of various fascinating applications in data storage systems, spintronics, microelectronics, and sensors has been explored [4–7]. BiFeO<sub>3</sub> shows highly distorted rhombohedral (*R3c*) perovskite structure at room temperature and *G*-type antiferromagnetic ordering, which originates from the super exchange interactions between the neighboring half-filled *d* orbital of the Fe<sup>3+</sup> cation and the occupied *2p* orbital of the O<sup>2-</sup> anion [8]. Recently, exploiting these properties, a low energy consuming nonvolatile magnetoelectric spin-orbit device has been proposed [9]. However, the high leakage current due to low resistivity, low saturation magnetization, low remanent magnetization, and weak magnetoelectric coupling in BiFeO<sub>3</sub> are the issues to be addressed before its realistic applications in next generation logic and memory devices [1,10–12]. The

interplay among the crystal structure, charge, spin, and orbital degrees of freedom provides a fertile research ground for improving the multiferroic properties in BFO [7,13,14]. Modifying the crystal structure, spin ordering, and band gap are keys to acquiring better electrical and magnetic properties. Various approaches including the elemental substitution at the *A* and/or *B* sites, high quality crystal formation, reducing the particle size, and heterostructure and solid solution formation have turned out to be very effective to improve the multiferroic properties of BFO [8,15,16]. Although promising, the multiferroicity and magnetoelectric coupling in either single phase BFO or composite/heterostructure require further improvement for its practical implementation, which demands more fundamental understanding of its structure-property correlation and its exploitation.

In this work, an experimental investigation combined with the theoretical calculations using density functional theory (DFT) and Monte Carlo simulation (MCS) were performed on the magnetic and electric properties of the (1–*x*)BFO+(*x*)La<sub>2</sub>NiMnO<sub>6</sub> (LNMO) (*x* = 0.0, 0.1, 0.2, and 0.3) composites. The double perovskite oxide LNMO is another widely studied below room temperature ferromagnetic semiconductor (Curie temperature  $T_C \sim 280$  K) with rich physical properties [17–18]. In our previous study we observed that the large lattice parameter mismatches between BFO and LNMO lattices makes both the lattices highly strained and pushes the BFO lattice from being regular rhombohedral (*R3c*) to the lowest possible triclinic (*P1*) phase [19]. Previously, Chen *et al.* observed the formation of ferroelectric triclinic phase in the mixed phase regions of highly strained BiFeO<sub>3</sub> thin film and predicted large piezoelectric response

\*Present address: Department of Materials Science and Engineering, University of Wisconsin Madison, 1509 University Ave, Madison WI 53706, USA.

<sup>†</sup>These authors contributed equally to this work.

<sup>‡</sup>Corresponding author: sarifulsekh@gmail.com

<sup>§</sup>Corresponding author: physics.tushar@gmail.com

in it [20]. Although the synthesis of multiferroic BFO based composites/heterostructures is a very effective approach to improve their multiferroic properties, most of the studies are on the regular rhombohedral and strain-mediated monoclinic, orthorhombic, and tetragonal BFO systems [21–23]. But, the magnetic and electric properties of triclinic BFO are yet to be fully explored. To get a fundamental insight into the electronic properties, we also performed the DFT calculation on triclinic BFO and compared it with that of rhombohedral BFO.

The combined experimental and theoretical study demonstrates that triclinic BFO structure (*P1*) has the promising potential to overcome the low magnetism, weak magnetodielectric coupling, and high leakage current of rhombohedral BiFeO<sub>3</sub>. The modified structure of BFO (*P1*) possesses increased electrical resistivity, and an increased spin canting resulting in significantly enhanced magnetization compared to the conventional *R3c* BFO.

The remaining part of this paper is organized as follows. In Sec. II, we report the experimental details. In Sec. III, we present the main results and discussions on the findings. Our conclusions based on the obtained results are summarized in Sec. IV, while the sample preparation, Monte Carlo simulation method, DFT calculation details, and spontaneous polarization calculations results are presented in the Appendices A, B, C, and D, respectively.

## II. METHODOLOGY

The composites are synthesized using the sol-gel method, and a description of the materials synthesis and pellet preparation procedure is presented in Appendix A. The electrical measurements are performed using circular discs (8 mm diameter and  $\sim 1$  mm thick) of the BFO/LNMO composites. A vibrating sample magnetometer (EverCool Quantum Design VSM magnetometer, Lakeshore) is used to study the magnetization of the as-prepared pellets in the temperature range from 80 to 400 K at zero field and an applied magnetic field of 5 kOe. The magnetic hysteresis properties are studied at 80 and 300 K. For the electrical measurements, the pellets were polished on both sides and silver electrodes were deposited using ultrapure silver paste (Ladd Research Industries Inc.). The capacitance (*C*) and conductance (*G*) were measured in the frequency range from 42 Hz to 1.6 MHz and in the temperature range 303 to 683 K using an LCR meter (3532-50, Hioki). The real part of the complex dielectric constant ( $\epsilon' = C/C_0$ , where  $C_0 = \epsilon_0 A/t$ ,  $\epsilon_0$  is the

permittivity of free space, *t* is the pellet thickness, and *A* is the surface area), imaginary part ( $\epsilon'' = Gx/\omega\epsilon_0$ ,  $\omega$  is the angular frequency) of the complex dielectric constant, dielectric loss factor ( $\tan\delta = \epsilon''/\epsilon'$ ), and AC electrical conductivity ( $\sigma = Gx$ ,  $x = t/A$ ) were obtained from the frequency dependence of *C* and *G*.

The electronic structure of BiFeO<sub>3</sub> was investigated using the full potential linearized augmented plane wave as implemented in the WIEN2K code [24,25]. The generalized gradient approximation (GGA) with the Hubbard parameter (*U*) method was used to study the spin polarized electronic band structure. The threshold energy between valence and core states is fixed to  $-7$  Ry for both triclinic and rhombohedral structures. The energy and charge cutoff are set to  $10^{-4}$  Ry and  $10^{-3} e$  for the self-consistent convergence in the self-consistent field (scf) cycles. The effective *U* value for the strong correlation between Fe-3*d* orbital electrons is set to 6 eV for both the cases. The temperature dependent magnetic properties of BFO/LNMO composite are analyzed through the Monte Carlo simulation method [26]. We considered the anisotropic three-dimensional Ising model for the simulation, and the Hamiltonian with nearest neighbor (nn) is described as

$$H = - \sum_{\langle i,j \rangle} J_{ij} s_i s_j - \Delta \sum_i s_i^2 - h \sum_i s_i,$$

where  $s_i$  and  $s_j$  are the spins at lattice sites *i* and *j* respectively.  $\sum_{\langle i,j \rangle}$  is the summation made over spin pairs coupled through the nn interaction constant  $J_{ij}$  and the magnetocrystalline anisotropy energy constant ( $\Delta$ ), and *h* is the external magnetic field applied along the *z* axis. The detailed Monte Carlo simulation and DFT calculations methods are described in Appendices B and C, respectively.

## III. RESULTS AND DISCUSSION

### A. Structural property

The detailed structural characteristics are reported in our previous work [19], and a summary of the crystal structures and lattice parameters of the BFO phases are presented in Table I and Fig. 1. The pure BiFeO<sub>3</sub> ( $x = 0.0$ ) is crystallized in the usual rhombohedral (space group *R3c*;  $a = b = c = 5.643$  Å,  $\alpha = \beta = 90^\circ$ ,  $\gamma = 120^\circ$ ) phase as shown in Fig. 1(a). But in the BFO/LNMO composite BFO is crystallized in the triclinic (space group *P1*;  $a = 3.931$  Å,  $b = 3.936$  Å,  $c = 3.956$  Å,  $\alpha = 90.32^\circ$ ,  $\beta = 90.24^\circ$ ,  $\gamma = 89.98^\circ$ ) phase as shown in Fig. 1(b). Figure 1(c) shows a qualitative comparison of the unit cell shape of the BFO structures. The

TABLE I. Lattice parameters of the BiFeO<sub>3</sub> phases in the  $(1-x)\text{BiFeO}_3 + (x)\text{La}_2\text{NiMnO}_6$  composites [19].

Lattice parameter	$x = 0.0$	$x = 0.1$	$x = 0.2$	$x = 0.3$
	BFO ( <i>R3c</i> )	BFO ( <i>P1</i> )	BFO ( <i>P1</i> )	BFO ( <i>P1</i> )
<i>a</i> (Å)	5.643	3.931	3.907	3.881
<i>b</i> (Å)	5.643	3.936	3.952	3.939
<i>c</i> (Å)	5.643	3.956	3.928	3.914
Cell volume (Å <sup>3</sup> )	125.18	61.34	60.85	59.86
Average Fe-O bond length (Å)	2.01	2.039	2.0496	2.043
Average FeO <sub>6</sub> octahedra volume (Å <sup>3</sup> )	10.845	10.224	10.142	9.987

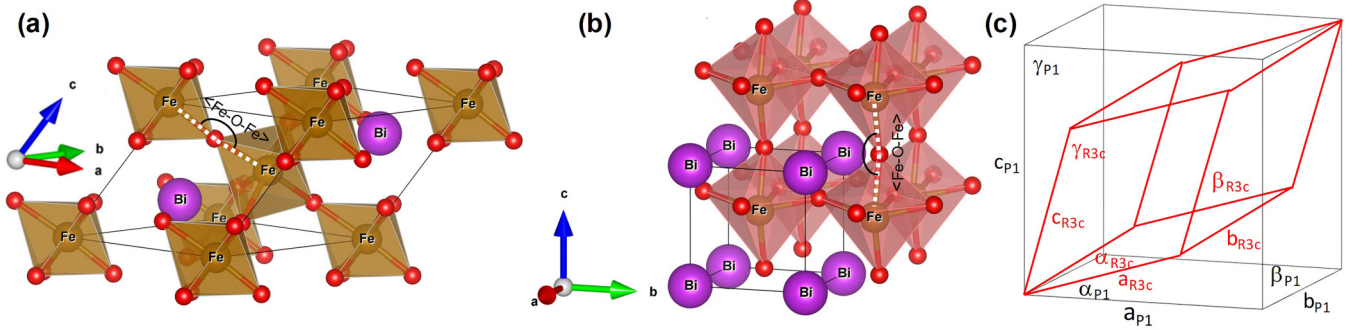


FIG. 1. Unit cell representation of (a) rhombohedral BFO and (b) triclinic BFO. (c) Comparison of unit cells of  $R3c$  (red) and  $P1$  (black) BFO structure.

double perovskite oxide LNMO is crystallized in the ordered monoclinic structure, which is further supported by the magnetic study, as discussed in Sect. IIIC. We also observed similar strain mediated structural transition in multiferroic KNbO<sub>3</sub>/LNMO composite, where the large lattice strain due to the lattice parameter mismatch transformed orthorhombic KNbO<sub>3</sub> to its cubic perovskite structure [27].

### B. Electrical conductivity

Figure 2(a) shows the logarithmic angular frequency,  $\log(\omega)$  dependence of the AC conductivity,  $\sigma(\omega)$ , which exhibits typical semiconductor behavior with a plateau in the low frequency region. The conductivity value in the low frequency plateau is nearly equal to the DC conductivity value ( $\sigma_{DC}$ ) and the conduction mechanism is also similar to its DC conduction mechanism, i.e., long range translational hopping of the thermally generated charge carriers from one localized site to another [28]. With the increase in frequency the probability of successful long range hopping decreases and the probability of short range hopping increases. As the frequency exceeds the critical hopping frequency ( $\omega_H$ ), the ratio of the long range to short range hopping starts to decrease, which results in a dispersive conductivity in the higher frequency region.  $\sigma(\omega)$  can be fitted and explained by the following Jonscher power law [29,30]:

$$\sigma(\omega) = \sigma_{dc} \left[ 1 + \left( \frac{\omega}{\omega_H} \right)^n \right],$$

where  $n$  is a dimensionless parameter varying from 0 to 1. The fitted values of  $\sigma_{DC}$ ,  $\omega_H$ , and  $n$  are shown in Table II. The value of the critical frequency  $\omega_H$  increases as the LNMO loading increases in the system as compared to the pure rhombohedral BFO. The conduction in BFO is governed by the Fe cation and oxygen vacancy [31]. The oxygen vacancy formation during the synthesis process causes reduction of a fraction of Fe<sup>3+</sup> cations and the formation of Fe<sup>2+</sup>. The Fe<sup>2+</sup> cations act as the trap center within the BFO lattice and are considered responsible for the large leakage current. The interaction between thermally released electrons and phonons in a polar medium such as BFO result in the formation of localized small polarons within the BFO lattice [32,33]. The slow motion of the small polarons between the nearest neighboring sites of BFO causes lattice distortion, considered as polaron hopping. With increment in frequency the occupancy of the trap center is reduced, and the density of the localized electrons increases, making them available for conduction. Hence the conductivity of the semiconductor system increases with frequency, as observed in Fig. 2(a).

The resistivity values ( $1/\sigma_{DC}$ ) obtained from the  $\sigma_{DC}$  values are plotted in Fig. 2(b), which shows that with the LNMO loading the resistivity of the samples increases up to  $x = 0.2$ . This resistivity change may be attributed to the structural transformation from rhombohedral ( $R3c$ ) BFO to triclinic ( $P1$ ) BFO. The electronic structure and electrical properties in  $ABO_3$  perovskites are determined by the hybridisation strength between Fe and O atoms in the FeO<sub>6</sub> octahedra.

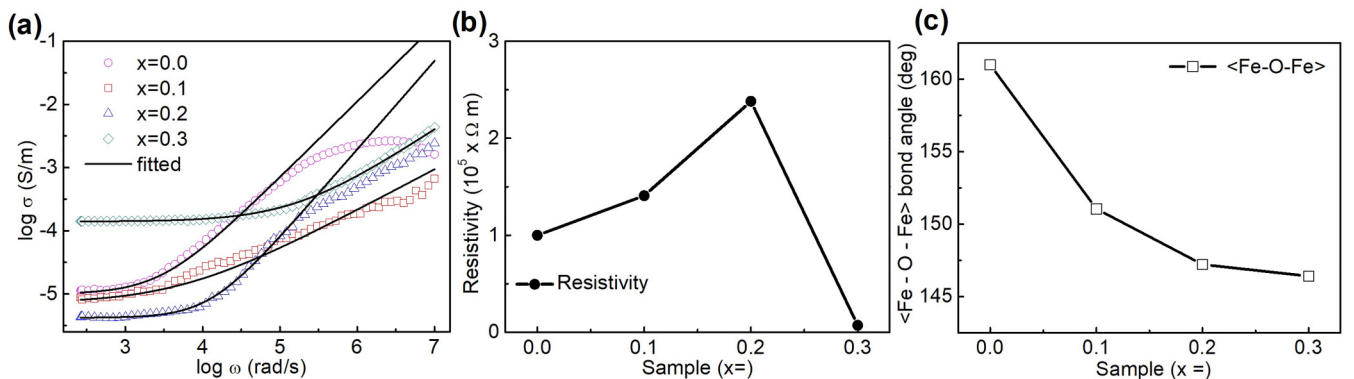


FIG. 2. (a) Logarithmic angular frequency dependence of AC conductivity. Solid lines indicate the power-law fitted data. (b) Room temperature DC conductivity, and (c)  $\langle \text{Fe-O-Fe} \rangle$  bond angle plot as a function of LNMO molar concentration.

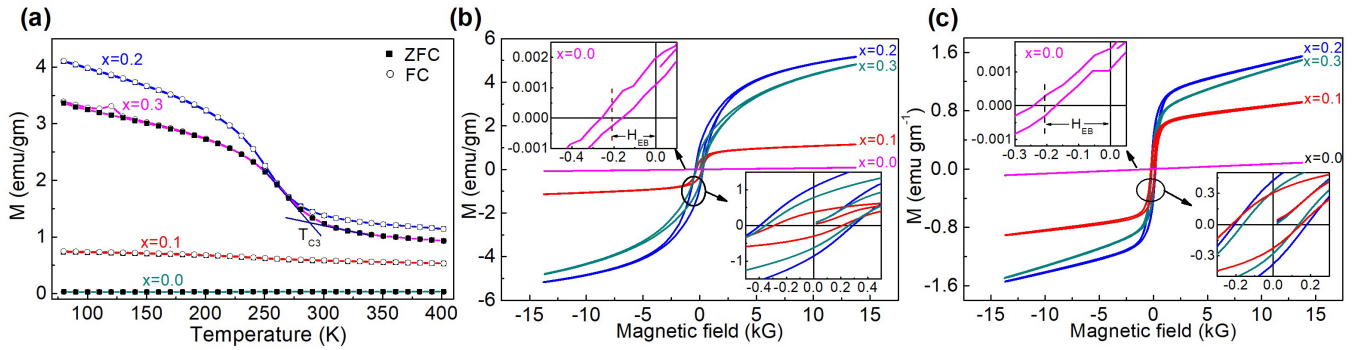


FIG. 3. (a) Temperature dependent magnetization plots in both zero-field cooling and field cooling conditions (5 kG); experimental  $M$ - $H$  loop at (b) 80 K and (c) 300 K. The figures in the insets have the same units as the main figure.

Figure 2(c) shows that the (Fe-O-Fe) bond angle, which plays a crucial role in the magnetic and electric properties of BFO, significantly decreases from rhombohedral to triclinic BFO in the composites. The reduced (Fe-O-Fe) bond angle decreases the hybridization strength between Fe-3*d* and O-2*p* orbitals in triclinic BFO, which is responsible for the increased resistivity in the composites. On the other hand, the excess loading of the relatively narrow band gap LNMO forms interconnected electrical networks which results in the reduced resistivity for  $x = 0.3$ .

### C. Magnetic property

The low temperature dependence of the magnetization plots (in the temperature range 80–400 K) [Fig. 3(a)] of the samples at 5 kG shows a large increment in the magnetization in the composites as compared to the pure rhombohedral BFO. A sudden rise in the magnetization at temperature  $\sim 280$  K has been observed in the composites as the temperature decreases, which is related to the ferromagnetic transition of LNMO. In general, the LNMO lattice offers the long-range ordering of both Ni and Mn cations, and forms the ordered monoclinic ( $P2_1/n$ ) or rhombohedral ( $R\bar{3}m$ ) structure and disordered orthorhombic ( $Pbnm$ ) phase [34,35]. Ordered LNMO phases have  $Ni^{2+}/Mn^{4+}$  oxidation states, and the  $Ni^{2+}-O-Mn^{4+}$  superexchange interaction generates ferromagnetism with the Curie temperature ( $T_{CM} \sim 280$  K) just below room temperature. The disordered LNMO phase has trivalent  $Ni^{3+}/Mn^{3+}$  oxidation states, and the  $Ni^{3+}-O-Mn^{3+}$  vibronic superexchange interaction incorporates ferromagnetism with a lower  $T_{CM}(\sim 150$  K) [36]. Hence, the Curie temperature [ $T_C \sim 280$  K, as shown in Fig. 3(a)] suggests the existence of an ordered LNMO phase in the composites, and the magnetic contribution above 280 K is completely attributed to another

source of origin, which is in this case the triclinic BFO phase. The plots of the magnetization ( $M$ ) as a function of magnetic field ( $H$ ) at temperatures 80 and 300 K are shown in Figs. 3(b) and 3(c), respectively. Pure BFO presents the simple linear  $M(H)$  dependence with very small remanent magnetization ( $M_r$ ) and saturation magnetization. The summaries of the magnetic parameters at 300 and 80 K are tabulated in Tables III and IV. It is noteworthy that a large increment in the magnetization has been observed in the composites. The remanent magnetizations for the samples with  $x = 0.0, 0.1, 0.2,$  and  $0.3$  are 0.0003, 0.304, 0.425, 0.332 emu/g m, respectively. The room temperature remanent magnetizations in the samples with  $x = 0.1, 0.2,$  and  $0.3$  are increased by almost 1000, 1400, and 1100 times, respectively, as compared to the pure BFO. The room temperature magnetization at 14 kG for the samples  $x = 0.0, 0.1, 0.2,$  and  $0.3$  are 0.09, 0.92, 1.55, 1.50 emu/g m, respectively. The magnetizations for the samples  $x = 0.1, 0.2,$  and  $0.3$  are increased by 10.2, 17.2, and 16.6 times, respectively. The comparison of the room temperature remanent magnetization of (0.8BFO + 0.2LNMO) with some other reported BFO based bulk samples, as tabulated in Table V, suggests that this triclinic BFO has much higher magnetization as compared to other phases of BFO. However, the lowering of BFO concentration may be the reason for decreasing magnetization in the sample with  $x = 0.3$ . The overall increment in magnetization in the composites may be because of the triclinic crystal structure of BFO. The magnetization in multiferroic BFO depends on the antiferromagnetic sublattice angularity, with the Dzyaloshinski-Moriya interaction (DM) playing the key role. The DM interaction leads to the spin canting, resulting in the appearance of a rather small total ferromagnetic (FM) moment in an antiferromagnetic

TABLE II. Jonscher power-law fitting parameters.

Sample	$\sigma_{DC} \times 10^4$ (S/cm)	$\omega_H$ (rad/s)	$n$
$x = 0.0$	10.0	2900	0.9
$x = 0.1$	14.1	5500	0.91
$x = 0.2$	23.8	12500	0.3
$x = 0.3$	71.4	165000	0.8

TABLE III. Magnetic parameters derived from the experimental and Monte Carlo (M-C) simulated  $M$ - $H$  hysteresis loop at 300 K.

Sample	$M_r$ (emu/gm)		$M_s$ (emu/gm)		$H_{cr}$ (emu/gm)	
	Expt.	M-C	Expt.	M-C	Expt.	M-C
$x = 0.0$	0.0003	0.000024	0.088	0.004	0.035	0.007
$x = 0.1$	0.304	0.020	0.922	0.913	0.188	0.137
$x = 0.2$	0.425	0.480	1.551	1.167	0.195	0.149
$x = 0.3$	0.332	0.32	1.498	1.409	0.149	0.091

TABLE IV. Magnetic parameters derived from the experimental and Monte Carlo (M-C) simulated  $M$ - $H$  hysteresis loop at 80 K.

Sample	$M_r$ (emu/gm)		$M_s$ (emu/gm)		$H_{cr}$ (emu/gm)	
	Expt.	M-C	Expt.	M-C	Expt.	M-C
$x = 0.0$	0.0005	0.0008	0.087	0.092	0.051	0.096
$x = 0.1$	0.383	0.404	1.149	0.61	0.252	0.486
$x = 0.2$	1.076	4.029	5.17	4.04	0.347	2.486
$x = 0.3$	0.766	3.406	4.822	3.417	0.302	1.452

(AFM) structure, thus enhancing the magnetism. Here the decreased (Fe-O-Fe) bond angle in the triclinic BFO increases the canting of spins and, hence, improves the magnetization as compared to the  $R3c$  BFO [37–39].

#### D. Monte Carlo simulations of magnetic properties

In our study, we also performed Monte Carlo simulations using the Metropolis algorithm to investigate the magnetic properties of BFO/LNMO solid solutions; the detailed calculation formalism is described in Appendix B [46–48]. As shown in Fig. 4(a), the simulated temperature-dependent magnetization plots of the systems follow the same pattern as the experimental data. This indicates that our simulations accurately capture the magnetic behavior of the systems under investigation. Figure 4(b) shows that the  $M$ - $H$  loops at 80 K manifest the FM nature of the composites compared to the AFM  $R3c$  BFO. Therefore, the FM nature of the composites may be attributed to the FM nature of LNMO and triclinic BFO. Furthermore, we have also investigated the effect of external magnetic fields on the room temperature hysteresis loops of the BFO/LNMO composite systems. The simulated MH loops above the Curie temperature of LNMO, i.e., at 300 K, as shown in Fig. 4(c) also suggest the ferromagnetic nature of the solid solutions, which is consistent with the FM nature of  $P1$  BFO. Moreover, the simulations showed a considerable increase in magnetization compared to pure BFO, which is qualitatively consistent with the experimental data as represented in Tables III and IV. These findings

highlight the success of our Monte Carlo simulations in accurately reproducing the temperature-dependent magnetization behavior and the influence of external magnetic fields on the BFO/LNMO composite systems.

#### E. Dielectric properties

We also studied the temperature dependent dielectric constant ( $\epsilon'$ ) of samples  $x = 0$  and  $0.2$  to qualitatively check the magnetoelectric coupling. The appearance of a dielectric anomaly near the magnetic transition temperature of a multiferroic material indicates the presence of the multiferroic magnetoelectric coupling [49]. If  $\epsilon'$  shows a minute anomaly at the magnetic transition temperature, the dielectric property of this material is generally less sensitive to the magnetic field. As the ferroelectric and magnetic ordering in BiFeO<sub>3</sub> are associated with different ions Bi and Fe, respectively, the multiferroic coupling in BiFeO<sub>3</sub> is relatively weak [50]. The temperature dependent dielectric constant plots of the rhombohedral BFO and the composite with  $x = 0.2$ , as shown in Fig. 5(a), reveal the dielectric anomaly near the magnetic transition temperature, suggesting the presence of the magnetoelectric coupling below 640 K in these materials. Interestingly, the composite with  $x = 0.2$  shows a significantly enhanced dielectric anomaly near the magnetic transition temperature at around 640 K, suggesting much stronger magnetoelectric coupling in it compared to the  $R3c$  BFO. But more research on the spin structure–property correlation of triclinic BFO is required to understand this behavior. We have also calculated the dielectric loss tangent ( $\tan\delta$ ), which quantitatively denotes the dissipation of electrical and electromagnetic energy (e.g., heat) due to different physical process such as electrical charge transport, dielectric relaxation, resonant transition, and nonlinear dielectric effects in a dielectric medium [51]. The dielectric loss tangent also shows the anomaly near the magnetic transition temperature, which is consistent with the dielectric constant plot. The dielectric loss tangents,  $\tan\delta$ , of samples with  $x = 0$  and  $x = 0.2$  as shown in Fig. 5(b) demonstrate nearly similar energy dissipation up to 400 K, and much lower dielectric loss in the composite with  $x = 0.2$  as compared to  $x = 0$  above 400 K. Overall, these experimental studies reveal the significantly higher magnetization and stronger magnetoelectric coupling in the triclinic

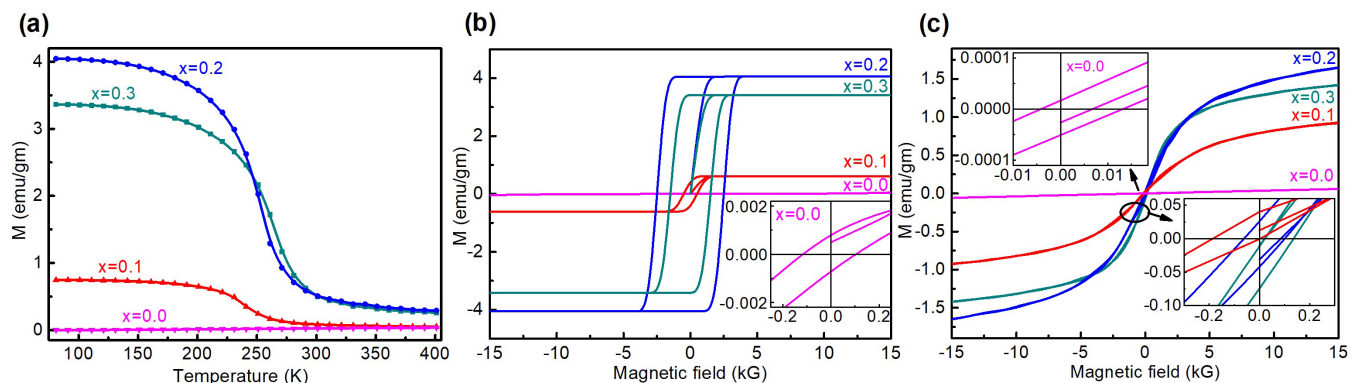


FIG. 4. (a) Monte Carlo simulation of magnetization versus temperature. Monte Carlo simulated  $M$ - $H$  loop at (b) 80 K and (c) 300 K. The figures in the insets have the same units as the main figure.

TABLE V. Comparison of the magnetic moment of sample with  $x = 0.2$  with some recent bulk BFO based magnetic materials.

Material	$M_r$ (emu/gm)	Year	Temperature
0.8BFO + 0.2LNMO	0.425	This work	300 K
0.7BFO + 0.3TbMnO <sub>3</sub> [40]	~ 0.15	2019	275 K
Bi <sub>0.95</sub> Gd <sub>0.05</sub> FeO <sub>3</sub> [41]	0.218	2019	RT
Bi <sub>1-x</sub> Ca <sub>x</sub> FeO <sub>3</sub> ( $x = 0.1$ ) [42]	0.096	2019	RT
0.8(Bi <sub>0.9</sub> La <sub>0.1</sub> FeO <sub>3</sub> ) - 0.2(KBr) [43]	~ 0.25	2019	300 K
BiFe <sub>1-x</sub> Se <sub>x</sub> O <sub>3</sub> , $x = 0.25$ [44]	0.034	2019	300 K
Bi <sub>0.92</sub> La <sub>0.08</sub> Fe <sub>1-x</sub> Se <sub>x</sub> O <sub>3</sub> , $x = 0$ [44]	0.1334	2019	300 K
Bi <sub>0.5</sub> La <sub>0.5</sub> Fe <sub>0.5</sub> Mn <sub>0.5</sub> O <sub>3</sub> [45]	0.7 (Much lower at RT)	2017	2 K

BFO based composite, motivating us to further explore this triclinic BFO structure using the DFT calculation formalism.

### F. Density functional theory calculations

We have studied the band structure, density of states (DOS), magnetic moments, and spontaneous polarization in both  $R3c$  and  $P1$  BFO, which are described below. The spin polarized band structure of the rhombohedral BFO is shown in Figs. 6(a) and 6(b), and the band structure of triclinic BFO is presented in Figs. 6(c) and 6(d). The DFT calculated lowest band gap for the  $R3c$  BFO phase for both the spin-up and spin-down conditions is 1.92 eV, consistent with the experimental direct band gap of bulk rhombohedral BFO ( $\sim 2$ eV) [52]. On the other hand, the triclinic phase has band gaps of 2.25 and 2.22 eV, as observed in the spin-up and spin-down conditions, respectively. The lowest band gap in  $P1$  BFO is in the down spin channel [Fig. 6(d)] which is higher than the  $R3c$  BFO. In the nonoptical applications of multiferroic materials electron can jump from valence band to conduction band via thermal excitation i.e., by phonon absorption. As phonons have zero spin, the electron generally conserves its spin during thermal excitation from the valence band to the conduction band. Hence the lowest energy gap for  $P1$  BFO for the non-spin-flip thermal excitation is 2.2 eV, higher than that of  $R3c$  BFO (1.92 eV). Hence, due to the wider energy gap, the triclinic BFO is expected to possess higher resistivity than the rhombohedral BFO, which is consistent with the experimental DC conductivity study. This observed higher resistance may help to reduce the leakage current

of BFO, which has been a main shortcoming of BFO for its device use. Interestingly, the spin-flip optical bandgap of  $P1$  BFO is 1.56 eV, which is lower than that of the  $R3c$  BFO (1.92 eV). Besides multiferroism, in recent years BFO has shown promising potential for various photosensing applications including solar cells, photoelectrochemical water splitting, etc. [28,53,54]. However, its efficiency in the photosensing devices is limited due to the wide optical band gap and related poor visible light absorbance of  $R3c$  BFO. Hence,  $P1$  BFO with its relatively narrower optical band gap, which is much closer to the Shockley-Queisser band gap ( $\sim 1.34$  eV) [55], could significantly enhance the performance of BFO in photo sensing devices.

Figure 7(a) and 7(b) display the spin-polarized DOS for the  $R3c$  and  $P1$  structures of BFO, respectively. Upon analyzing the partial DOS, it becomes evident that the densities in the valence band maximum (VBM) and conduction band minimum (CBM) are primarily dominated by the Fe-3d and O-2p states, with a minor contribution from the Bi-6p state in both the  $R3c$  and  $P1$  structures of BFO. However, it is noteworthy that the overlap between the O-2p and Fe-3d states is more pronounced in the triclinic BFO structure compared to the rhombohedral BFO structure. This observation suggests a stronger covalent nature of the Fe-O bonds in the triclinic BFO configuration. The spin-polarized symmetric DOS of  $R3c$  BFO reveals its conventional AFM phase. On the other hand, the spin-polarized asymmetric DOS of  $P1$  BFO again confirms its FM nature, consistent with the experimental results. In terms of magnetic moments, the calculated values for the Bi, Fe, and O atoms in

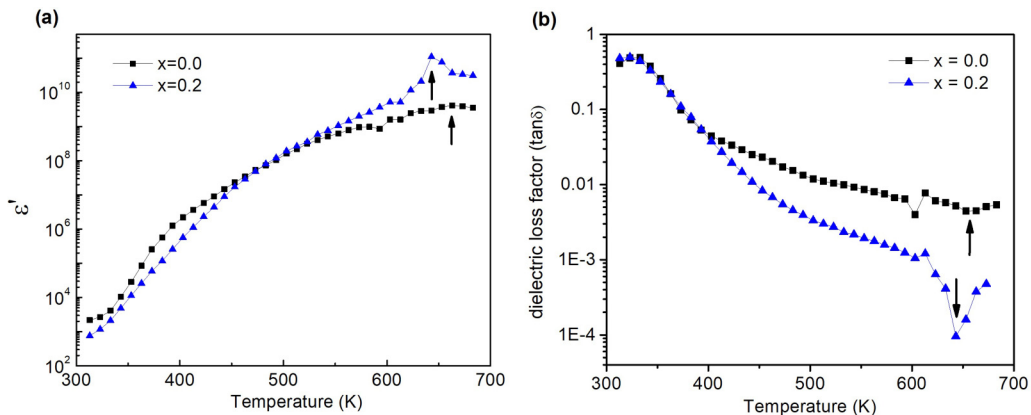


FIG. 5. (a) Temperature dependence of the real part of the dielectric constant ( $\epsilon'$ ), and (b) dielectric loss factor at frequency 4.8 MHz.

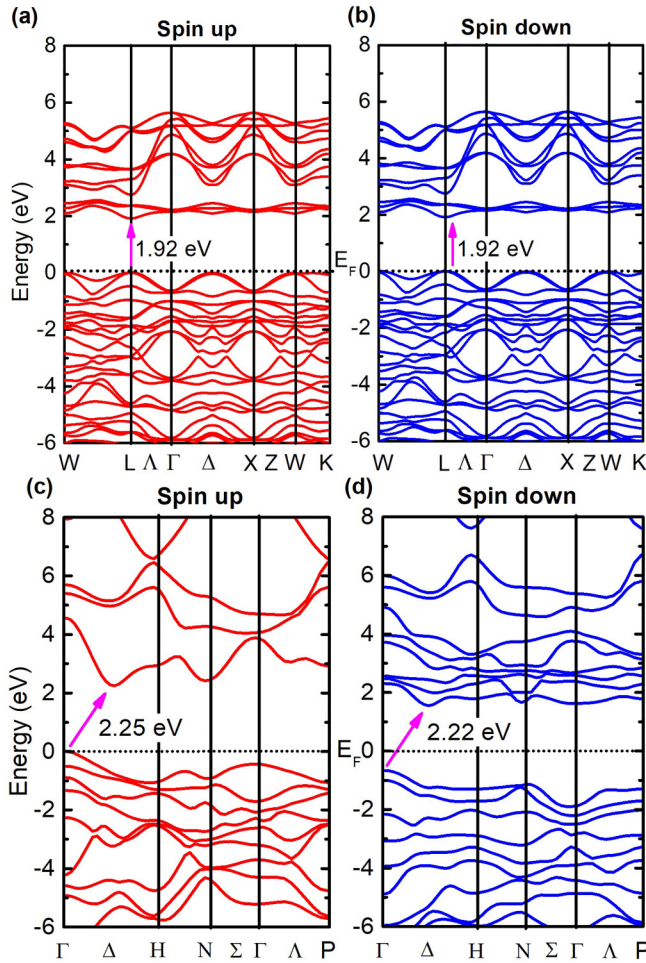


FIG. 6. Band structure of rhombohedral BFO for (a) spin up and (b) spin down configurations. Band structure of triclinic BFO for (c) spin up and (d) spin down configurations.

the rhombohedral BFO structure are found to be  $0.049 \mu_B$  ( $\pm 0.027$  emu/gm),  $3.56 \mu_B$  ( $\pm 355.85$  emu/gm), and  $0.33 \mu_B$  ( $\pm 16.75$  emu/gm), respectively. It is worth mentioning that the calculated magnetic moment of the  $\text{Fe}^{3+}$  ion is consistent with both previous experimental and theoretical results. A low-temperature neutron-diffraction study conducted on the  $R3c$  BFO structure reported a measured magnetic moment for the  $\text{Fe}^{3+}$  ion of  $3.75 \mu_B$  (374.85 emu/gm) [56], which aligns closely with the calculated value reported in this work. Additionally, a previous DFT study also demonstrated that the magnetic moment of the  $\text{Fe}^{3+}$  ion in the  $R3c$  BFO structure is approximately  $3.65 \mu_B$  (364.85 emu/gm) [57].

In the triclinic  $P1$  structure of BFO, the spin magnetic moments for the Bi, Fe, and O atoms are determined to be  $0.014 \mu_B$  (0.373 emu/gm),  $3.97 \mu_B$  (412.83 emu/gm), and  $0.19 \mu_B$  (41.87 emu/gm), respectively. A comparison of the DFT calculated magnetic moments of both  $R3c$  and  $P1$  BFO is presented in Table VI. These values indicate an increased magnetic moment in the triclinic BFO structure compared to rhombohedral structure. The theoretical spin-only magnetic moment for the  $\text{Fe}^{3+}$  ion is calculated to be  $5.91 \mu_B$  (590.76 emu/gm), based on the formula  $\sqrt{n(n+2)}$ , where  $n$  represents the number of unpaired electrons. However, the

TABLE VI. DFT calculated magnetic moments of  $R3c$  and  $P1$  BFO.

Ion	$R3c$ (emu/gm)	$P1$ (emu/gm)
$\text{Bi}^{3+}$	$\pm 0.03$	0.37
$\text{Fe}^{3+}$	$\pm 355.85$	412.83
$\text{O}^{2-}$	$\pm 16.75$	41.87
Interstitial	0.00	29.77
Cell	0.00	356.88

calculated magnetic moment from DFT calculations is found to be lower than the theoretical value. This deviation can be attributed to the hybridization between the Fe-3d and O-2p orbitals, where the five 3d electrons of  $\text{Fe}^{3+}$  do not localize on the atomic orbitals but rather form Wannier orbitals, where the presence of spin nonpolarized O 2p states makes a notable contribution which affects the magnetic moment [58].

To visualize the magnetic spin structure, ground state magnetic properties of  $R3c$  and  $P1$  structures were determined using DFT calculations as depicted in Figs. 7(c) and 7(d). These figures provide a representation of the spatial distribution and orientation of the magnetic spins in the materials, aiding in the understanding of its magnetic behaviour. These findings further provide valuable insights into the spin-polarized DOS and magnetic moments of BFO in both the crystal structures. Overall, the analysis of the magnetic moments and spin structures in the triclinic BFO structure shed light on its magnetic properties and effects of orbital hybridization on magnetic moment.

In summary, the strain mediated triclinic ( $P1$ ) BFO phase demonstrated enhanced magnetism along with increased resistance and magnetoelectric coupling as compared to the regular  $R3c$  BFO phase. Hence, the next focus should be on the strain-mediated synthesis of 2D triclinic BFO on a suitable lattice matched substrate and its exploration. The 2D triclinic BFO based heterostructure is expected to demonstrate improved resistivity, high saturation magnetization, remanence magnetization, and robust magnetoelectric coupling which is essential for the practical implementation of room temperature multiferroic technology.

#### IV. CONCLUSIONS

Studies on the electronic and magnetic properties of the composite BFO/LNMO were performed, and the combined experimental and theoretical analysis demonstrates the remarkable improvement of the magnetization and multiferroic magnetoelectric coupling in the composites as compared to rhombohedral BFO. The enhanced room temperature magnetization and resistivity in the composites are attributed to the triclinic BFO phase. Interestingly, triclinic BFO has decreased (Fe-O-Fe) bond angle and an increased spin canting, which result in the significantly increased resistivity and enhanced magnetization, respectively, as compared to the regular BFO ( $R3c$ ) structure. Overall, this study introduces triclinic BFO ( $P1$ ) phase as a promising pathway to realize room temperature multiferroic material and opens a new avenue to overcome the limiting factors of the current multiferroic technology.

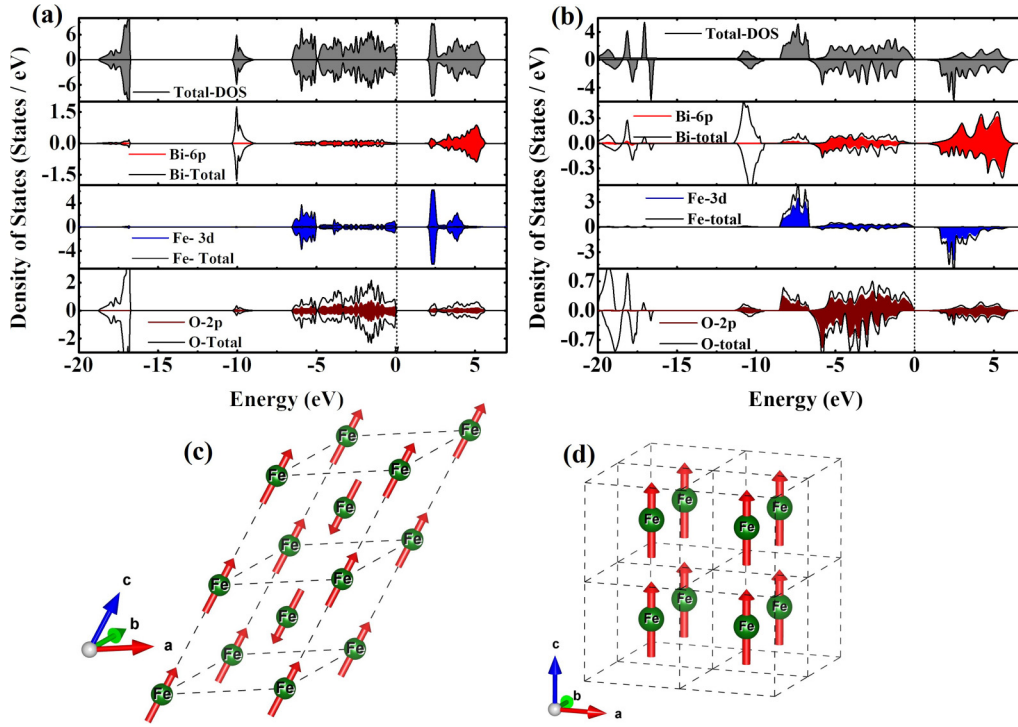


FIG. 7. Spin polarized DOS and PDOS of (a) *R3c* and (b) *P1* BFO. Ground state magnetic structure of (c) *R3c* and (d) *P1* BiFeO<sub>3</sub> derived from DFT calculation.

#### ACKNOWLEDGMENTS

M.S.S. and T.K.B. would like to thank the Department of Science and Technology (DST), Government of India for providing the financial support in form of the INSPIRE Fellowship (IF150220 and No. IF160418, respectively).

#### APPENDIX A: $(1-x)$ BFO + $(x)$ LNMO ( $x = 0.0, 0.1, 0.2, 0.3$ ) SYNTHESIS AND PELLET PREPARATION

The multiferroic composite  $(1-x)$ BFO +  $(x)$ LNMO (with  $x = 0.0, 0.1, 0.2,$  and  $0.3$ ) powders were prepared using the sol-gel method [19]. First, the reagent grade metal nitrates,  $\text{Bi}(\text{NO}_3)_3 \cdot 5\text{H}_2\text{O}$ ,  $\text{Fe}(\text{NO}_3)_3 \cdot 6\text{H}_2\text{O}$ ,  $\text{La}(\text{NO}_3)_3 \cdot 3\text{H}_2\text{O}$ ,  $\text{Ni}(\text{NO}_3)_2 \cdot 4\text{H}_2\text{O}$ , and  $\text{Mn}(\text{NO}_3)_2 \cdot 6\text{H}_2\text{O}$  were dissolved in 2-methoxy ethanol solvent. 3% of extra  $\text{Bi}(\text{NO}_3)_3 \cdot 5\text{H}_2\text{O}$  was taken to avoid the Bi evaporation loss during the heating process. A solution of tartaric acid in 2-methoxy ethanol (in 1:1 molar ratio with the metal nitrates) was added dropwise in the first solution and mixed well. The well mixed solutions were dried at 393 K to get the black precursor powder. Finally, the precursor powders were heated in an

ambient furnace in a two-step heating method. In the first step, the samples were heated at 723 K for 2 hours to ensure the complete phase formation of BFO. In the second step, the furnace temperature was gradually increased to 923 K from 723 K and heated for 5 hours to ensure the complete double perovskite phase formation of LNMO. Finally, the furnace was cooled down to the room temperature at a cooling rate of 1 K/min. The synthesised powders were pelletized into circular discs of average diameter 100 mm and thickness 2 mm using polyvinyl alcohol as the binder and sintered at 973 K for 3 hours for the magnetic and dielectric measurements.

#### APPENDIX B: MODEL AND MONTE CARLO SIMULATION DETAILS

The temperature dependent magnetic properties of BFO/LNMO composite were analyzed through the Monte Carlo simulation method. For the triclinic BFO structure, we considered only one magnetic ion,  $\text{Fe}^{3+}$ , at corner edges [26]. We used the anisotropic 3D Ising model for the simulation; other models such as the Heisenberg model do not satisfy the experimental data as accurately. The anisotropic 3D Ising

TABLE VII. Lattice parameters used for the DFT calculations (before and after energy minimization).

Symmetry	Condition	$a$ (Å)	$b$ (Å)	$c$ (Å)	$\alpha$ (deg)	$\beta$ (deg)	$\gamma$ (deg)
BFO ( <i>R3c</i> )	Before	5.5872	5.5872	13.8907	90	90	120
	After	5.5216	5.5216	13.7287	90	90	120
BFO ( <i>P1</i> )	Before	3.93100	3.93100	3.9310	90.3200	90.2400	89.9800
	After	3.93104	3.93104	3.93104	90.3194	90.2443	89.9762



model Hamiltonian with nearest neighbor (nn) is

$$H = - \sum_{\langle i,j \rangle} J_{ij} s_i s_j - \Delta \sum_i s_i^2 - h \sum_i s_i,$$

where  $s_i$  and  $s_j$  are the spins at lattice sites  $i$  and  $j$  respectively.  $\sum_{\langle i,j \rangle}$  are the summations made over spin pairs coupled through the nn interaction constant  $J_{ij}$ , and the magnetocrystalline anisotropy energy constant ( $\Delta$ ) – 24.8  $\mu\text{eV}/\text{Fe}$  is taken from a previous study [59] and  $h$  is the external magnetic field applied along the  $z$  axis. For the complex perovskite  $(1-x)(\text{BFO}) + x(\text{LNMO})$  ( $x = 0.1, 0.2, 0.3$ ), we have taken two sublattices; one is for BiFeO<sub>3</sub> and another for La<sub>2</sub>NiMnO<sub>6</sub>. The whole complex perovskite consists of the three magnetic ions Fe<sup>3+</sup>, Ni<sup>2+</sup>, and Mn<sup>4+</sup>. So, there are six spin-spin interactions present in the system and the interaction constants are  $J_{\text{Fe-Fe}}$ ,  $J_{\text{Ni-Ni}}$ ,  $J_{\text{Mn-Mn}}$ ,  $J_{\text{Ni-Mn}}$ ,  $J_{\text{Fe-Ni}}$ , and  $J_{\text{Fe-Mn}}$ . But, the interactions between Fe-Ni and Fe-Mn are very small due to the small concentration of LNMO and large atomic distance between these atoms. So, the nearest-neighbor interaction constants are  $J_{(\text{Fe-Fe})}$ ,  $J_{(\text{Ni-Mn})}$ ,  $J_{(\text{Ni-Ni})}$ , and  $J_{(\text{Mn-Mn})}$ . BFO has antiferromagnetic ordering temperature ( $T_N$ ) around 640 K [60]. The LNMO has a paramagnetic to ferromagnetic transition around 280 K upon cooling. So, the interactions between Ni-Ni, Mn-Mn, and Ni-Mn are ferromagnetic. Masrou *et al.* determined the interaction constants for LNMO from the mean-field theoretical calculations [61]. We have taken the spin magnitudes of Fe<sup>3+</sup>, Ni<sup>2+</sup> and Mn<sup>4+</sup> as 5/2, 1, and 3/2 respectively. For pure BFO, we determined the interaction constants from the mean field approximation. The formula is given by

$$T_N = \frac{2}{3K_B} ZS(S+1)J_{\text{Fe-Fe}},$$

where  $Z$  is the coordination number and  $S$  is the spin value of all magnetic ions.  $T_N$  denotes the experimental value of the transition temperature and  $J_{\text{Fe-Fe}}$  is the interaction constant and  $K_B$  is the Boltzmann constant. For the pure  $R3c$  BFO the reported transition temperature is 640 K. The calculated value of  $J_{\text{Fe-Fe}}$  in the case of the  $R3c$  BFO turns out to be 18.28 K. For the composite materials, we have calculated the interaction constant from the mean-field approximation formula,  $T_C = \frac{2}{3K_B} ZS(S+1)J$ . The transition temperatures  $T_C$  in the composites were determined from their temperature dependent magnetization data, as shown in Fig. 3(a). For  $x = 0.1$ , we found the experimental  $T_{C1} = 276\text{K}$ , and the calculated values of the coupling constants are  $J_{\text{Fe-Fe}} = 7.8\text{K}$ ,  $J_{\text{Ni-Ni}} = 34.5\text{K}$ ,  $J_{\text{Mn-Mn}} = 18.4\text{K}$ ,  $J_{\text{Ni-Mn}} = 26.1\text{K}$ . For  $x = 0.2$  ( $T_{C2} = 280\text{K}$ ), we found the values of  $J_{\text{Fe-Fe}} = 8\text{K}$ ,  $J_{\text{Ni-Ni}} = 35.01\text{K}$ ,  $J_{\text{Mn-Mn}} = 18.7\text{K}$ ,  $J_{\text{Ni-Mn}} = 26.5\text{K}$ . In the case of  $x = 0.3$ , the experimental  $T_{C3} = 286\text{K}$ , and we calculated the values of  $J_{\text{Fe-Fe}} = 8.2\text{K}$ ,  $J_{\text{Ni-Ni}} = 35.75\text{K}$ ,  $J_{\text{Mn-Mn}} = 19.07\text{K}$ ,  $J_{\text{Ni-Mn}} = 27.08\text{K}$ .

The magnetic properties of the BFO and BFO/LNMO composites are analysed using MCS under the Metropolis algorithm using the above-described Hamiltonian with cyclic boundary conditions on the lattice [62,63]. We performed this MCS on a sample of dimension  $N = L \times L \times L$ , where  $L$  is the number of unit cells in all three directions. We used  $N = 32 \times 32 \times 32$  number of lattices for these simulations. The single-spin-flip mechanism is used for all lattice sites to

minimize the internal energy, and the flips of these spin values are accepted or rejected according to the Boltzmann statistics [63]. At each temperature for every spin configuration, 10<sup>5</sup> Monte Carlo steps were performed to equilibrate the lattice and the next 10<sup>6</sup> steps for thermal averaging of the total magnetization,  $M = \frac{1}{N} \langle \sum_i s_i \rangle$ , where the sum is performed over all spin values of Fe<sup>3+</sup>, Ni<sup>2+</sup>, and Mn<sup>4+</sup>, and  $\langle \dots \rangle$  indicates the statistical time average.

### APPENDIX C: DFT CALCULATION METHOD

The electronic structure of BiFeO<sub>3</sub> was investigated using the full potential linearized augmented plane wave as implemented in the WIEN2K code [23,24]. The generalized gradient approximation (GGA) with the Hubbard parameter ( $U$ ) method was used to study the spin polarized electronic band structure. The threshold energy between valence and core states is fixed to  $-7$  Ry for both triclinic and rhombohedral structures. The maximum angular momentum,  $l_{\text{max}}$  for the wave function expansion inside the atomic spheres is set at 10 and the plane wave cutoff  $R_{\text{MT}} \times K_{\text{Max}}$  is taken to 7 Ry with 1000  $k$  points mesh integration over the first Brillouin zone to solve the Kohn-Sham equations. Here,  $R_{\text{MT}}$  and  $K_{\text{Max}}$  stand for the average muffin-tin radii of the ionic sphere and the wave function cutoff. The muffin-tin radii of BFO under the triclinic  $P1$  space group are 2.16, 1.69, and 1.46 Å for Bi, Fe, and O atoms, respectively. For rhombohedral  $R3c$  they are 2.5, 1.9, and 1.63 Å, respectively. The energy and charge cutoff are set to  $10^{-4}$  Ry and  $10^{-3} e$  for the self-consistent convergence in the scf cycles. The effective  $U$  value for the strong correlation between Fe-3d orbital electrons is set to 6 eV for both cases. The structural optimization has been done to find the stabilized lattice parameter of the crystal structures. The initial and optimized values of lattice parameters of both structures are shown in Table VII.

We employed the QUANTUM ESPRESSO package [64] to perform calculations concerning the spontaneous polarization. The projector augmented-wave (PAW) method was utilized, along with the GGA based on the Perdew-Burke-Ernzerhof (PBE) functional, to account for exchange-correlation effects. A plane-wave energy cutoff of 75 Ry was set for the scf calculation. For geometry optimization and electronic structure calculations, a  $7 \times 7 \times 7$  Monkhorst-Pack  $k$ -point mesh was employed. Addressing the strong Coulomb repulsion ( $U$ ) occurring between the localized  $d$  states of Fe, we incorporated the GGA+Hubbard potential ( $U$ ) approach to appropriately describe correlation effects within transition metal oxides. In this study, a Hubbard potential  $U$  value of 6 eV was applied to Fe after careful consideration.

### APPENDIX D: DFT CALCULATION OF SPONTANEOUS POLARISATION

Spontaneous polarization stands as a major ferroelectric property of BFO. Hence, it is imperative to examine the spontaneous polarization of this material. In this study, we computed the spontaneous polarization by considering the combined contributions of electronic and ionic polarizations. The DFT calculated polarisation and tilting angle in both the  $R3c$  and  $P1$  BFO are represented in Figs. 8(a)–8(d). In the case of  $R3c$ -structured BFO, the spontaneous polarization arises

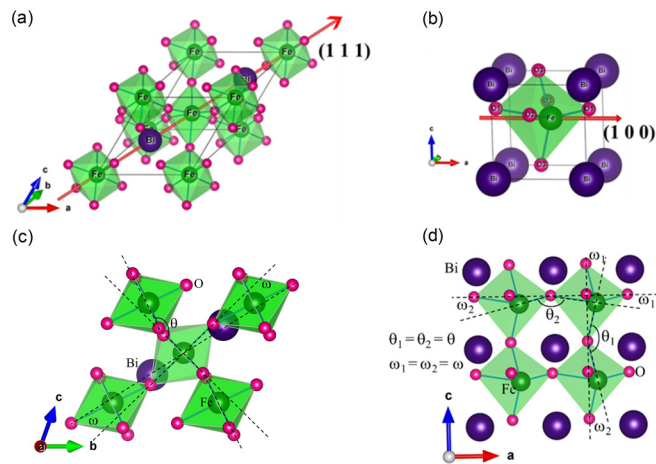


FIG. 8. (a) The polarization direction of Bi atoms and FeO<sub>6</sub> octahedra along (111) and (b) (100) directions for  $R3c$  and  $P1$  BFO structures respectively. (c) The octahedral tilting angle  $\omega$  and Fe-O-Fe bond angle  $\theta$  for  $R3c$  BFO. (d) The octahedral tilting angle  $\omega$  and Fe-O-Fe bond angle  $\theta$  with respect to directions parallel to the  $a$  axis and  $c$  axis for  $P1$  BFO.

from the displacement of Bi, Fe, and O atoms along the [111] direction [65]. Conversely,  $P1$  BFO exhibits polarization along the [100] direction. This spontaneous polarization can be attributed to the electronic hybridization between the  $6s$  electronic states of Bi, and the  $2s$  and  $2p$  states of O. This hybridization results in a stereo chemically active polarizable lone pair of Bi atoms, giving rise to the observed spontaneous polarization [66,67]. The QUANTUM ESPRESSO software utilizing the PBE sol pseudopotential was employed to compute the total spontaneous polarization. The calculated spontaneous polarization values are  $72$  and  $102 \mu\text{C}/\text{cm}^2$  for  $R3c$  and  $P1$  BFO, respectively. The spontaneous polarization is shown schematically in Figs. 8(a) and 8(b) for  $R3c$  BFO and  $P1$  BFO respectively. Our computed polarization values of  $R3c$  BFO fall within the range of some previously reported theoretical results of  $R3c$  BFO:  $87.8 \mu\text{C}/\text{cm}^2$  [68],  $90.9 \mu\text{C}/\text{cm}^2$  [69], and  $57.34 \mu\text{C}/\text{cm}^2$  [70]. Interestingly, our calculations reveal much higher spontaneous polarization in the triclinic BFO as compared to the conventional rhombohedral BFO. Figures 8(c) and 8(d) show the tilting angle  $\omega$  with respect to the directions parallel to  $a$  and  $b$  crystallographic axes of the FeO<sub>6</sub> octahedra and the Fe-O-Fe bond angle  $\theta$  [71]. The  $P1$  BFO structure is more tilted than the  $R3c$  BFO structure.

- [1] W.-R. Geng, Y.-L. Tang, Y.-L. Zhu, Y.-J. Wang, B. Wu, L.-X. Yang, Y.-P. Feng, M.-J. Zou, T.-T. Shi, Y. Cao, and X.-L. Ma, Magneto–electric–optical coupling in multiferroic BiFeO<sub>3</sub>-based films, *Adv. Mater.* **34**, 2106396 (2022).
- [2] Y. L. Huang, D. Nikonov, C. Addiego, R. V. Chopdekar, B. Prasad, L. Zhang, J. Chatterjee, H. J. Liu, A. Farhan, Y. H. Chu, M. Yang, M. Ramesh, Z. Q. Qiu, B. D. Huey, C. C. Lin, T. Gosavi, J. Iniguez, J. Bokor, X. Pan, I. Young, L. W. Martin, and R. Ramesh, Manipulating magnetoelectric energy landscape in multiferroics, *Nat. Commun.* **11**, 2836 (2020).
- [3] D. Sando, A. Barthelemy, and M. Bibes, BiFeO<sub>3</sub> epitaxial thin films and devices: Past, present and future, *J. Phys.: Condens. Matter* **26**, 473201 (2014).
- [4] G. Catalan and J. F. Scott, Physics and applications of bismuth ferrite, *Adv. Mater.* **21**, 2463 (2009).
- [5] D. Yi, P. Yu, Y. C. Chen, H. H. Lee, Q. He, Y. H. Chu, and R. Ramesh, Tailoring Magnetoelectric Coupling in BiFeO<sub>3</sub>/La<sub>0.7</sub>Sr<sub>0.3</sub>MnO<sub>3</sub> Heterostructure through the Interface Engineering, *Adv. Mater.* **31**, 1806335 (2019).
- [6] J. H. Lee, H. J. Choi, D. Lee, M. G. Kim, C. W. Bark, S. Ryu, M.-A. Oak, and H. M. Jang, Variations of ferroelectric off-centering distortion and  $3d-4p$  orbital mixing in La-doped BiFeO<sub>3</sub> multiferroics, *Phys. Rev. B* **82**, 045113 (2010).
- [7] L. Yin and W. Mi, Progress in BiFeO<sub>3</sub>-based heterostructures: Materials, properties and applications, *Nanoscale* **12**, 477 (2020).
- [8] J. Silva, A. Reyes, H. Esparza, H. Camacho, and L. Fuentes, BiFeO<sub>3</sub>: A review on synthesis, doping and crystal structure, *Integr. Ferroelectr.* **126**, 47 (2011).
- [9] S. Manipatruni, D. E. Nikonov, C. C. Lin, T. A. Gosavi, H. Liu, B. Prasad, Y.-L. Huang, E. Bonturim, R. Ramesh, and I. A. Young, Scalable energy-efficient magnetoelectric spin–orbit logic, *Nature (London)* **565**, 35 (2019).
- [10] A. Haykal, J. Fischer, W. Akhtar, J. Y. Chauleau, D. Sando, A. Finco, F. Godel, Y. A. Birkholzer, C. Carretero, N. Jaouen, M. Bibes, M. Viret, S. Fusil, V. Jacques, and V. Garcia, Antiferromagnetic textures in BiFeO<sub>3</sub> controlled by strain and electric field, *Nat. Commun.* **11**, 1704 (2020).
- [11] N. A. Spaldin and R. Ramesh, Advances in magnetoelectric multiferroics, *Nat. Mater.* **18**, 203 (2019).
- [12] C. R. Joshi, M. Acharya, G. J. Mankey, and A. Gupta, Effect of thickness and frequency of applied field on the switching dynamics of multiferroic bismuth ferrite thin films, *Phys. Rev. Mater.* **6**, 054409 (2022).
- [13] L. Yin, X. Wang, and W. Mi, Tunable review on synthesis, doping and crystal strain BiXO<sub>3</sub>/BiIrO<sub>3</sub> (X = Fe, Mn) Ferroelectric Superlattices, *ACS Appl. Mater. Interfaces* **10**, 3822 (2018).
- [14] R. Zhang, P. Hu, L. Bai, X. Xie, H. Dong, M. Wen, Z. Mu, X. Zhanga, and F. Wu, New multiferroic BiFeO<sub>3</sub> with large polarization, *Phys. Chem. Chem. Phys.* **24**, 5939 (2022).
- [15] S. Saha, R. P. Singh, Y. Liu, A. B. Swain, A. Kumar, V. Subramanian, A. Arockiarajan, G. Srinivasan, and R. Ranjan, Strain transfer in ferroelectric-ferrimagnetic magnetoelectric composite, *Phys. Rev. B* **103**, L140106 (2021).
- [16] N. Wang, X. Luo, L. Han, Z. Zhang, R. Zhang, H. Olin, and Y. Yang, Structure, performance, and application of BiFeO<sub>3</sub> nanomaterials, *Nano-Micro Lett.* **12**, 81 (2020).
- [17] R. I. Dass, J. Q. Yan, and J. B. Goodenough, Oxygen stoichiometry, ferromagnetism, and transport properties of La<sub>2-x</sub>NiMnO<sub>6+δ</sub>, *Phys. Rev. B* **68**, 064415 (2003).
- [18] M. S. Sheikh, D. Ghosh, A. Dutta, S. Bhattacharyya, and T. P. Sinha, Lead free double perovskite oxides Ln<sub>2</sub>NiMnO<sub>6</sub> (Ln = La, Eu, Dy, Lu), a new promising material for photovoltaic application, *Mater. Sci. Eng.: B* **226**, 10 (2017).
- [19] M. S. Sheikh, D. Ghosh, T. K. Bhowmik, A. Dutta, S. Bhattacharyya, and T. P. Sinha, When multiferroics become

- photoelectrochemical catalysts: A case study with BiFeO<sub>3</sub>/La<sub>2</sub>NiMnO<sub>6</sub>, *Mater. Chem. Phys.* **244**, 122685 (2020).
- [20] Z. Chen, S. Prosandeev, Z. L. Luo, W. Ren, Y. Qi, C. W. Huang, L. You, C. Gao, I. A. Kornev, T. Wu, J. Wang, P. Yang, T. Sritharan, L. Bellaiche, and L. Chen, Coexistence of ferroelectric triclinic phases in highly strained BiFeO<sub>3</sub> films, *Phys. Rev. B* **84**, 094116 (2011).
- [21] M. R. Walden, C. V. Ciobanu, and G. L. Brennecke, Density-functional theory calculation of magnetic properties of BiFeO<sub>3</sub> and BiCrO<sub>3</sub> under epitaxial strain, *J. Appl. Phys.* **130**, 104102 (2021).
- [22] B. Xu, S. Meyer, M. J. Verstraete, L. Bellaiche, and B. Dupé, First-principles study of spin spirals in the multiferroic BiFeO<sub>3</sub>, *Phys. Rev. B* **103**, 214423 (2021).
- [23] F. Sun, D. Chen, X. Gao, and J.-M. Liu, Emergent strain engineering of multiferroic BiFeO<sub>3</sub> thin films, *J. Materiomics*. **7**, 281 (2021).
- [24] P. Blaha, K. Schwarz, F. Tran, R. Laskowski, G. K. H. Madsen, and L. D. Marks, WIEN2k, An APW+lo program for calculating the properties of solids, *J. Chem. Phys.* **152**, 074101 (2020).
- [25] P. Blaha, K. Schwarz, P. Sorantin, and S. Trickey, Full-potential, linearized augmented plane wave programs for crystalline systems, *Comput. Phys. Commun.* **59**, 399 (1990).
- [26] S. Yahyaoui, S. Kallel, and H. T. Diep, Magnetic properties of perovskites La<sub>0.7</sub>Sr<sub>0.3</sub>Mn<sub>0.7</sub><sup>3+</sup>Mn<sub>0.3-x</sub><sup>4+</sup>Ti<sub>x</sub>O<sub>3</sub>: Monte Carlo simulation versus experiments, *J. Magn. Magn. Mater.* **416**, 441 (2016).
- [27] Md. S. Sheikh, A. Dutta, T. K. Bhowmik, S. K. Ghosh, S. K. Rout, and T. P. Sinha, Synthesis, structural and photo physical properties of perovskite oxide (KNbO<sub>3</sub>)<sub>1-x</sub> + (La<sub>2</sub>NiMnO<sub>6</sub>)<sub>x</sub> for photovoltaic application, in *35th European Photovoltaic Solar Energy Conference and Exhibition, Brussels, 2018* (EU PVSEC, Munich, 2018), pp. 143–148.
- [28] M. B. Mohamed, H. Wang, and H. Fuess, Dielectric relaxation and magnetic properties of Cr doped GaFeO<sub>3</sub>, *J. Phys. D: Appl. Phys.* **43**, 455409 (2010).
- [29] A. K. Jonscher, *Dielectric Relaxation in Solids*, (Chelsea Dielectrics, London, 1983).
- [30] E. F. Hairetdinov, N. F. Uvarov, H. K. Patel, and S. W. Martin, Estimation of the free-charge carrier concentration in fast-ion conducting Na<sub>2</sub>S–B<sub>2</sub>S<sub>3</sub> glasses from an analysis of the frequency-dependent conductivity, *Phys. Rev. B* **50**, 13259 (1994).
- [31] G. W. Pabst, L. W. Martin, Y.-H. Chu, and R. Ramesh, Leakage mechanisms in BiFeO<sub>3</sub> thin films, *Appl. Phys. Lett.* **90**, 072902 (2007).
- [32] A. Radmilovic, T. J. Smart, Y. Ping, and K.-S. Choi, Combined experimental and theoretical investigations of n-type BiFeO<sub>3</sub> for use as a photoanode in a photoelectrochemical cell, *Chem. Mater.* **32**, 3262 (2020).
- [33] G. Geneste, C. Paillard, and B. Dkhil, Polarons, vacancies, vacancy associations, and defect states in multiferroic BiFeO<sub>3</sub>, *Phys. Rev. B* **99**, 024104 (2019).
- [34] M. S. Sheikh, A. P. Sakhya, A. Dutta, and T. P. Sinha, Light induced charge transport in La<sub>2</sub>NiMnO<sub>6</sub> based Schottky diode, *J. Alloys Compd.* **727**, 238 (2017).
- [35] N. S. Rogado, J. Li, A. W. Sleight, and M. A. Subramanian, Magnetocapacitance and magnetoresistance near room temperature in a ferromagnetic semiconductor: La<sub>2</sub>NiMnO<sub>6</sub>, *Adv. Mater.* **17**, 2225 (2005).
- [36] S. Zhao, L. Shia, S. Zhou, J. Zhao, H. Yang, and Y. Guo, Size-dependent magnetic properties and Raman spectra of La<sub>2</sub>NiMnO<sub>6</sub> nanoparticles, *J. Appl. Phys.* **106**, 123901 (2009).
- [37] N. Gao, C. Quan, Y. Ma, Y. Han, Z. Wu, W. Mao, J. Zhang, J. Yang, X. Li, and W. Huang, Experimental and first principles investigation of the multiferroics BiFeO<sub>3</sub> and Bi<sub>0.9</sub>Ca<sub>0.1</sub>FeO<sub>3</sub>: Structure, electronic, optical and magnetic properties, *Physica B* **481**, 45 (2016).
- [38] C. Ederer and N. A. Spaldin, Weak ferromagnetism and magnetoelectric coupling in bismuth ferrite, *Phys. Rev. B* **71**, 060401(R) (2005).
- [39] M. Rangi, A. Agarwal, S. Sanghi, R. Singh, S. S. Meena, and A. Das, Crystal structure and magnetic properties of Bi<sub>0.8</sub>A<sub>0.2</sub>FeO<sub>3</sub> (A = La, Ca, Sr, Ba) multiferroics using neutron diffraction and Mossbauer spectroscopy, *AIP Adv.* **4**, 87121 (2014).
- [40] P. K. Gupta, S. Ghosh, S. Kumar, A. Pal, P. Singh, M. Alam, A. Singh, S. Roy, R. Singh, B. P. Singh, N. N. Kumar, E. F. Schwier, M. Sawada, T. Matsumura, K. Shimada, H.-J. Lin, Y.-Y. Chin, A. K. Ghosh, and S. Chatterjee, Room temperature exchange bias in antiferromagnetic composite BiFeO<sub>3</sub> – TbMnO<sub>3</sub>, *J. Appl. Phys.* **126**, 243903 (2019).
- [41] M. A. Matin, M. N. Hossain, M. A. Hakim, and M. F. Islam, Effects of Gd and Cr co-doping on structural and magnetic properties of BiFeO<sub>3</sub> nanoparticles, *Mater. Res. Express* **6**, 055038 (2019).
- [42] H. Xian, L. Tang, Z. Mao, J. Zhang, and X. Chen, Bounded magnetic polarons induced enhanced magnetism in Ca-doped BiFeO<sub>3</sub>, *Solid State Commun.* **287**, 54 (2019).
- [43] D. V. Karpinsky, O. M. Fesenko, M. V. Silibin, S. V. Dubkov, M. Chaika, A. Yaremkevich, A. Lukowiak, Y. Gerasymchuk, W. Stręk, A. Pakalniškis, R. Skaudzius, A. Kareiva, Y. M. Fomichov, V. V. Shvartsman, S. V. Kalinin, N. V. Morozovsky, and A. N. Morozovska, Ferromagnetic-like behavior of Bi<sub>0.9</sub>La<sub>0.1</sub>FeO<sub>3</sub>–KBr nanocomposites, *Sci. Rep.* **9**, 10417 (2019).
- [44] S. Rizwan, M. Umar, Z. U. D. Babar, S. U. Awan, and M. A. Rehman, Selenium-enriched flower-like of bismuth ferrite nanosheets assembly with associated magnetic properties, *AIP Adv.* **9**, 055025 (2019).
- [45] R. Singh, P. K. Gupta, S. Kumar, A. G. Joshi, A. K. Ghosh, S. Patil, and S. Chatterjee, Enhancement in electrical and magnetic properties with Ti-doping in Bi<sub>0.5</sub>La<sub>0.5</sub>Fe<sub>0.5</sub>Mn<sub>0.5</sub>O<sub>3</sub>, *J. Appl. Phys.* **121**, 154101 (2017).
- [46] A. S. Erchidi Elyacoubi, R. Masrour, and A. Jabar, Magnetocaloric effect and magnetic properties in SmFe<sub>1-x</sub>Mn<sub>x</sub>O<sub>3</sub> perovskite: Monte Carlo simulations, *Solid State Commun.* **271**, 39 (2018).
- [47] P. Sharma, R. Masrour, A. Jabar, J. Fan, A. Kumar, L. Ling, C. Ma, C. Wang, and H. Yang, Structural and magnetocaloric properties of rare-earth orthoferrite perovskite: TmFeO<sub>3</sub>, *Chem. Phys. Lett.* **740**, 137057 (2020).
- [48] T. K. Bhowmik and T. P. Sinha, Al-dependent electronic and magnetic properties of YCrO<sub>3</sub> with magnetocaloric application: An ab-initio and Monte Carlo approach, *Physica B* **606**, 412659 (2021).
- [49] G. L. Yuan, Siu Wing, J. M. Liu, and Z. G. Liu, Structural transformation and ferroelectromagnetic behavior in

- single-phase  $\text{Bi}_{1-x}\text{Nd}_x\text{FeO}_3$  multiferroic ceramics, *Appl. Phys. Lett.* **89**, 052905 (2006).
- [50] S.-W. Cheong and M. Mostovoy, Multiferroics: A magnetic twist for ferroelectricity, *Nat. Mater.* **6**, 13 (2007).
- [51] V. L. Gurevich and A. K. Tagantsev, Intrinsic dielectric loss in crystals, *Advances Phys.* **40**, 719 (1991).
- [52] S. Sharma and M. Kumar, Band gap tuning and optical properties of  $\text{BiFeO}_3$  nanoparticles, *Mater. Today: Proc.* **28**, 168 (2020).
- [53] T. Choi, S. Lee, Y. J. Choi, V. Kiryukhin, and W. Cheong, Switchable ferroelectric diode and photovoltaic effect in  $\text{BiFeO}_3$ , *Science* **324**, 63 (2009).
- [54] Z. Li, Y. Zhao, W.-L. Li, R. Song, W. Zhao, Z. Wang, Y. Peng, and W.-D. Fei, *J. Phys. Chem. C* **125**, 9411 (2021).
- [55] S. Rühle, Tabulated values of the Shockley–Queisser limit for single junction solar cells, *Sol. Energy* **130**, 139 (2016).
- [56] I. Sosnowska, T. P. Neumaier, and E. Steichele, Spiral magnetic ordering in bismuth ferrite, *J. Phys. C: Solid State Phys.* **15**, 4835 (1982).
- [57] P. Hermet, M. Goffinet, J. Kreisel, and P. Ghosez, Raman and infrared spectra of multiferroic bismuth ferrite from first principles, *Phys. Rev. B* **75**, 220102(R) (2007).
- [58] S. V. Streltsov, Magnetic moment suppression in  $\text{Ba}_3\text{CoRu}_2\text{O}_9$ : Hybridization effect, *Phys. Rev. B* **88**, 024429 (2013).
- [59] J. T. Zhang, X. M. Lu, J. Zhou, H. Sun, J. Su, C. C. Ju, F. Z. Huang, and J. S. Zhu, Origin of magnetic anisotropy and spiral spin order in multiferroic  $\text{BiFeO}_3$ , *Appl. Phys. Lett.* **100**, 242413 (2012).
- [60] P. Fischer, M. Połomska, I. Sosnowska, and M. Szymanski, Temperature dependence of the crystal and magnetic structures of  $\text{BiFeO}_3$ , *J. Phys. C: Solid St. Phys.* **13**, 1931 (1980).
- [61] R. Masrour and J. Abderrahim, Magnetocaloric and magnetic properties of  $\text{La}_2\text{NiMnO}_6$  double perovskite, *Chin. Phys. B* **25**, 087502 (2016).
- [62] D. P. Landau and K. Binder, *A Guide to Monte Carlo Simulations in Statistical Physics*, 3rd ed. (Cambridge University Press, New York, 2009).
- [63] M. E. J. Newman and G. T. Barkema, *Monte Carlo Methods in Statistical Physics* (Oxford University Press, New York, 1999).
- [64] P. Giannozzi *et al.*, QUANTUM ESPRESSO: A modular and open-source software project for quantum simulations of materials, *J. Phys.: Condens. Matter.* **21**, 395502 (2009).
- [65] D. Lebeugle, D. Colson, A. Forget, and M. Viret, Very large spontaneous electric polarization in  $\text{BiFeO}_3$  single crystals at room temperature and its evolution under cycling fields, *Appl. Phys. Lett.* **91**, 022907 (2007).
- [66] P. Ravindran, R. Vidya, A. Kjekshus, H. Fjellvåg, and O. Eriksson, Theoretical investigation of magnetoelectric behavior in  $\text{BiFeO}_3$ , *Phys. Rev. B* **74**, 224412 (2006).
- [67] M. Tokunaga, M. Akaki, T. Ito, S. Miyahara, A. Miyake, H. Kuwahara, and N. Furukawa, Magnetic control of transverse electric polarization in  $\text{BiFeO}_3$ , *Nat. Commun.* **6**, 5878 (2015).
- [68] A. Stroppa and S. Picozzi, Hybrid functional study of proper and improper multiferroics, *Phys. Chem. Chem. Phys.* **12**, 5405 (2010).
- [69] M. Pugaczowa-Michalska and J. Kaczkowski, First-principles study of structural, electronic, and ferroelectric properties of rare-earth-doped  $\text{BiFeO}_3$ , *J. Mater. Sci.* **50**, 6227 (2015).
- [70] L. H. da S. Lacerda, R. A. P. Ribeiro, and S. R. de Lazaro, Magnetic, electronic, ferroelectric, structural and topological analysis of  $\text{AlFeO}_3$ ,  $\text{FeAlO}_3$ ,  $\text{FeVO}_3$ ,  $\text{BiFeO}_3$  and  $\text{PbFeO}_3$  materials: Theoretical evidences of magnetoelectric coupling, *J. Magn. Magn. Mater.* **480**, 199 (2019).
- [71] H. H'Môk, E. M. Aguilar, J. A. García, J. R. Ariño, L. Mestres, P. Alemany, D. H. Galván, J. M. S. Beltrones, and O. R. Herrera, Theoretical justification of stable ferromagnetism in ferroelectric  $\text{BiFeO}_3$  by first-principles, *Comput. Mater. Sci.* **164**, 66 (2019).